Fermilab-Pub-12-404-E

Search for the standard model Higgs boson in the $ZH \to \nu\bar{\nu}b\bar{b}$ channel in 9.5 fb^{-1} of $p\bar{p}$ collisions at $\sqrt{s} = 1.96$ TeV

V.M. Abazov,[32] B. Abbott,[69] B.S. Acharya,[26] M. Adams,[46] T. Adams,[44] G.D. Alexeev,[32] G. Alkhazov,[36] A. Alton[a],[58] G. Alverson,[57] A. Askew,[44] S. Atkins,[55] K. Augsten,[7] C. Avila,[5] F. Badaud,[10] L. Bagby,[45] B. Baldin,[45] D.V. Bandurin,[44] S. Banerjee,[26] E. Barberis,[57] P. Baringer,[53] J.F. Bartlett,[45] U. Bassler,[15] V. Bazterra,[46] A. Bean,[53] M. Begalli,[2] L. Bellantoni,[45] S.B. Beri,[24] G. Bernardi,[14] R. Bernhard,[19] I. Bertram,[39] M. Besançon,[15] R. Beuselinck,[40] P.C. Bhat,[45] S. Bhatia,[60] V. Bhatnagar,[24] G. Blazey,[47] S. Blessing,[44] K. Bloom,[61] A. Boehnlein,[45] D. Boline,[66] E.E. Boos,[34] G. Borissov,[39] T. Bose,[56] A. Brandt,[72] O. Brandt,[20] R. Brock,[59] A. Bross,[45] D. Brown,[14] J. Brown,[14] X.B. Bu,[45] M. Buehler,[45] V. Buescher,[21] V. Bunichev,[34] S. Burdin[b],[39] C.P. Buszello,[38] E. Camacho-Pérez,[29] B.C.K. Casey,[45] H. Castilla-Valdez,[29] S. Caughron,[59] S. Chakrabarti,[66] D. Chakraborty,[47] K.M. Chan,[51] A. Chandra,[74] E. Chapon,[15] G. Chen,[53] S. Chevalier-Théry,[15] D.K. Cho,[71] S.W. Cho,[28] S. Choi,[28] B. Choudhary,[25] S. Cihangir,[45] D. Claes,[61] J. Clutter,[53] M. Cooke,[45] W.E. Cooper,[45] M. Corcoran,[74] F. Couderc,[15] M.-C. Cousinou,[12] A. Croc,[15] D. Cutts,[71] A. Das,[42] G. Davies,[40] S.J. de Jong,[30,31] E. De La Cruz-Burelo,[29] F. Déliot,[15] R. Demina,[65] D. Denisov,[45] S.P. Denisov,[35] S. Desai,[45] C. Deterre,[15] K. DeVaughan,[61] H.T. Diehl,[45] M. Diesburg,[45] P.F. Ding,[41] A. Dominguez,[61] A. Dubey,[25] L.V. Dudko,[34] D. Duggan,[62] A. Duperrin,[12] S. Dutt,[24] A. Dyshkant,[47] M. Eads,[61] D. Edmunds,[59] J. Ellison,[43] V.D. Elvira,[45] Y. Enari,[14] H. Evans,[49] A. Evdokimov,[67] V.N. Evdokimov,[35] G. Facini,[57] L. Feng,[47] T. Ferbel,[65] F. Fiedler,[21] F. Filthaut,[30,31] W. Fisher,[59] H.E. Fisk,[45] M. Fortner,[47] H. Fox,[39] S. Fuess,[45] A. Garcia-Bellido,[65] J.A. García-González,[29] G.A. García-Guerra[c],[29] V. Gavrilov,[33] P. Gay,[10] W. Geng,[12,59] D. Gerbaudo,[63] C.E. Gerber,[46] Y. Gershtein,[62] G. Ginther,[45,65] G. Golovanov,[32] A. Goussiou,[76] P.D. Grannis,[66] S. Greder,[16] H. Greenlee,[45] G. Grenier,[17] Ph. Gris,[10] J.-F. Grivaz,[13] A. Grohsjean[d],[15] S. Grünendahl,[45] M.W. Grünewald,[27] T. Guillemin,[13] G. Gutierrez,[45] P. Gutierrez,[69] S. Hagopian,[44] J. Haley,[57] L. Han,[4] K. Harder,[41] A. Harel,[65] J.M. Hauptman,[52] J. Hays,[40] T. Head,[41] T. Hebbeker,[18] D. Hedin,[47] H. Hegab,[70] A.P. Heinson,[43] U. Heintz,[71] C. Hensel,[20] I. Heredia-De La Cruz,[29] K. Herner,[58] G. Hesketh[f],[41] M.D. Hildreth,[51] R. Hirosky,[75] T. Hoang,[44] J.D. Hobbs,[66] B. Hoeneisen,[9] J. Hogan,[74] M. Hohlfeld,[21] I. Howley,[72] Z. Hubacek,[7,15] V. Hynek,[7] I. Iashvili,[64] Y. Ilchenko,[73] R. Illingworth,[45] A.S. Ito,[45] S. Jabeen,[71] M. Jaffré,[13] A. Jayasinghe,[69] M.S. Jeong,[28] R. Jesik,[40] P. Jiang,[4] K. Johns,[42] E. Johnson,[59] M. Johnson,[45] A. Jonckheere,[45] P. Jonsson,[40] J. Joshi,[43] A.W. Jung,[45] A. Juste,[37] K. Kaadze,[54] E. Kajfasz,[12] D. Karmanov,[34] P.A. Kasper,[45] I. Katsanos,[61] R. Kehoe,[73] S. Kermiche,[12] N. Khalatyan,[45] A. Khanov,[70] A. Kharchilava,[64] Y.N. Kharzheev,[32] I. Kiselevich,[33] J.M. Kohli,[24] A.V. Kozelov,[35] J. Kraus,[60] S. Kulikov,[35] A. Kumar,[64] A. Kupco,[8] T. Kurča,[17] V.A. Kuzmin,[34] S. Lammers,[49] G. Landsberg,[71] P. Lebrun,[17] H.S. Lee,[28] S.W. Lee,[52] W.M. Lee,[45] X. Lei,[42] J. Lellouch,[14] D. Li,[14] H. Li,[11] L. Li,[43] Q.Z. Li,[45] J.K. Lim,[28] D. Lincoln,[45] J. Linnemann,[59] V.V. Lipaev,[35] R. Lipton,[45] H. Liu,[73] Y. Liu,[4] A. Lobodenko,[36] M. Lokajicek,[8] R. Lopes de Sa,[66] H.J. Lubatti,[76] R. Luna-Garcia[g],[29] A.L. Lyon,[45] A.K.A. Maciel,[1] R. Madar,[15] R. Magaña-Villalba,[29] S. Malik,[61] V.L. Malyshev,[32] Y. Maravin,[54] J. Martínez-Ortega,[29] R. McCarthy,[66] C.L. McGivern,[41] M.M. Meijer,[30,31] A. Melnitchouk,[60] D. Menezes,[47] P.G. Mercadante,[3] M. Merkin,[34] A. Meyer,[18] J. Meyer,[20] F. Miconi,[16] N.K. Mondal,[26] M. Mulhearn,[75] E. Nagy,[12] M. Naimuddin,[25] M. Narain,[71] R. Nayyar,[42] H.A. Neal,[58] J.P. Negret,[5] P. Neustroev,[36] H. Nguyen,[75] T. Nunnemann,[22] J. Orduna,[74] N. Osman,[12] J. Osta,[51] M. Padilla,[43] A. Pal,[72] N. Parashar,[50] V. Parihar,[71] S.K. Park,[28] R. Partridge[e],[71] N. Parua,[49] A. Patwa,[67] B. Penning,[45] M. Perfilov,[34] Y. Peters,[41] K. Petridis,[41] G. Petrillo,[65] P. Pétroff,[13] M.-A. Pleier,[67] P.L.M. Podesta-Lerma[h],[29] V.M. Podstavkov,[45] A.V. Popov,[35] M. Prewitt,[74] D. Price,[49] N. Prokopenko,[35] J. Qian,[58] A. Quadt,[20] B. Quinn,[60] M.S. Rangel,[1] K. Ranjan,[25] P.N. Ratoff,[39] I. Razumov,[35] P. Renkel,[73] I. Ripp-Baudot,[16] F. Rizatdinova,[70] M. Rominsky,[45] A. Ross,[39] C. Royon,[15] P. Rubinov,[45] R. Ruchti,[51] G. Sajot,[11] P. Salcido,[47] A. Sánchez-Hernández,[29] M.P. Sanders,[22] A.S. Santos[i],[1] G. Savage,[45] L. Sawyer,[55] T. Scanlon,[40] R.D. Schamberger,[66] Y. Scheglov,[36] H. Schellman,[48] S. Schlobohm,[76] C. Schwanenberger,[41] R. Schwienhorst,[59] J. Sekaric,[53] H. Severini,[69] E. Shabalina,[20] V. Shary,[15] S. Shaw,[59] A.A. Shchukin,[35] R.K. Shivpuri,[25] V. Simak,[7] P. Skubic,[69] P. Slattery,[65] D. Smirnov,[51] K.J. Smith,[64] G.R. Snow,[61] J. Snow,[68] S. Snyder,[67] S. Söldner-Rembold,[41] L. Sonnenschein,[18] K. Soustruznik,[6] J. Stark,[11] D.A. Stoyanova,[35] M. Strauss,[69] L. Suter,[41] P. Svoisky,[69] M. Takahashi,[41] M. Titov,[15] V.V. Tokmenin,[32]

Y.-T. Tsai,[65] K. Tschann-Grimm,[66] D. Tsybychev,[66] B. Tuchming,[15] C. Tully,[63] L. Uvarov,[36] S. Uvarov,[36] S. Uzunyan,[47] R. Van Kooten,[49] W.M. van Leeuwen,[30] N. Varelas,[46] E.W. Varnes,[42] I.A. Vasilyev,[35] P. Verdier,[17] A.Y. Verkheev,[32] L.S. Vertogradov,[32] M. Verzocchi,[45] M. Vesterinen,[41] D. Vilanova,[15] P. Vokac,[7] H.D. Wahl,[44] M.H.L.S. Wang,[45] J. Warchol,[51] G. Watts,[76] M. Wayne,[51] J. Weichert,[21] L. Welty-Rieger,[48] A. White,[72] D. Wicke,[23] M.R.J. Williams,[39] G.W. Wilson,[53] M. Wobisch,[55] D.R. Wood,[57] T.R. Wyatt,[41] Y. Xie,[45] R. Yamada,[45] S. Yang,[4] W.-C. Yang,[41] T. Yasuda,[45] Y.A. Yatsunenko,[32] W. Ye,[66] Z. Ye,[45] H. Yin,[45] K. Yip,[67] S.W. Youn,[45] J.M. Yu,[58] J. Zennamo,[64] T. Zhao,[76] T.G. Zhao,[41] B. Zhou,[58] J. Zhu,[58] M. Zielinski,[65] D. Zieminska,[49] and L. Zivkovic[71]

(The D0 Collaboration*)

[1]*LAFEX, Centro Brasileiro de Pesquisas Físicas, Rio de Janeiro, Brazil*
[2]*Universidade do Estado do Rio de Janeiro, Rio de Janeiro, Brazil*
[3]*Universidade Federal do ABC, Santo André, Brazil*
[4]*University of Science and Technology of China, Hefei, People's Republic of China*
[5]*Universidad de los Andes, Bogotá, Colombia*
[6]*Charles University, Faculty of Mathematics and Physics, Center for Particle Physics, Prague, Czech Republic*
[7]*Czech Technical University in Prague, Prague, Czech Republic*
[8]*Center for Particle Physics, Institute of Physics, Academy of Sciences of the Czech Republic, Prague, Czech Republic*
[9]*Universidad San Francisco de Quito, Quito, Ecuador*
[10]*LPC, Université Blaise Pascal, CNRS/IN2P3, Clermont, France*
[11]*LPSC, Université Joseph Fourier Grenoble 1, CNRS/IN2P3, Institut National Polytechnique de Grenoble, Grenoble, France*
[12]*CPPM, Aix-Marseille Université, CNRS/IN2P3, Marseille, France*
[13]*LAL, Université Paris-Sud, CNRS/IN2P3, Orsay, France*
[14]*LPNHE, Universités Paris VI and VII, CNRS/IN2P3, Paris, France*
[15]*CEA, Irfu, SPP, Saclay, France*
[16]*IPHC, Université de Strasbourg, CNRS/IN2P3, Strasbourg, France*
[17]*IPNL, Université Lyon 1, CNRS/IN2P3, Villeurbanne, France and Université de Lyon, Lyon, France*
[18]*III. Physikalisches Institut A, RWTH Aachen University, Aachen, Germany*
[19]*Physikalisches Institut, Universität Freiburg, Freiburg, Germany*
[20]*II. Physikalisches Institut, Georg-August-Universität Göttingen, Göttingen, Germany*
[21]*Institut für Physik, Universität Mainz, Mainz, Germany*
[22]*Ludwig-Maximilians-Universität München, München, Germany*
[23]*Fachbereich Physik, Bergische Universität Wuppertal, Wuppertal, Germany*
[24]*Panjab University, Chandigarh, India*
[25]*Delhi University, Delhi, India*
[26]*Tata Institute of Fundamental Research, Mumbai, India*
[27]*University College Dublin, Dublin, Ireland*
[28]*Korea Detector Laboratory, Korea University, Seoul, Korea*
[29]*CINVESTAV, Mexico City, Mexico*
[30]*Nikhef, Science Park, Amsterdam, the Netherlands*
[31]*Radboud University Nijmegen, Nijmegen, the Netherlands*
[32]*Joint Institute for Nuclear Research, Dubna, Russia*
[33]*Institute for Theoretical and Experimental Physics, Moscow, Russia*
[34]*Moscow State University, Moscow, Russia*
[35]*Institute for High Energy Physics, Protvino, Russia*
[36]*Petersburg Nuclear Physics Institute, St. Petersburg, Russia*
[37]*Institució Catalana de Recerca i Estudis Avançats (ICREA) and Institut de Física d'Altes Energies (IFAE), Barcelona, Spain*
[38]*Uppsala University, Uppsala, Sweden*
[39]*Lancaster University, Lancaster LA1 4YB, United Kingdom*
[40]*Imperial College London, London SW7 2AZ, United Kingdom*
[41]*The University of Manchester, Manchester M13 9PL, United Kingdom*
[42]*University of Arizona, Tucson, Arizona 85721, USA*
[43]*University of California Riverside, Riverside, California 92521, USA*
[44]*Florida State University, Tallahassee, Florida 32306, USA*
[45]*Fermi National Accelerator Laboratory, Batavia, Illinois 60510, USA*
[46]*University of Illinois at Chicago, Chicago, Illinois 60607, USA*
[47]*Northern Illinois University, DeKalb, Illinois 60115, USA*
[48]*Northwestern University, Evanston, Illinois 60208, USA*
[49]*Indiana University, Bloomington, Indiana 47405, USA*
[50]*Purdue University Calumet, Hammond, Indiana 46323, USA*

[51] University of Notre Dame, Notre Dame, Indiana 46556, USA
[52] Iowa State University, Ames, Iowa 50011, USA
[53] University of Kansas, Lawrence, Kansas 66045, USA
[54] Kansas State University, Manhattan, Kansas 66506, USA
[55] Louisiana Tech University, Ruston, Louisiana 71272, USA
[56] Boston University, Boston, Massachusetts 02215, USA
[57] Northeastern University, Boston, Massachusetts 02115, USA
[58] University of Michigan, Ann Arbor, Michigan 48109, USA
[59] Michigan State University, East Lansing, Michigan 48824, USA
[60] University of Mississippi, University, Mississippi 38677, USA
[61] University of Nebraska, Lincoln, Nebraska 68588, USA
[62] Rutgers University, Piscataway, New Jersey 08855, USA
[63] Princeton University, Princeton, New Jersey 08544, USA
[64] State University of New York, Buffalo, New York 14260, USA
[65] University of Rochester, Rochester, New York 14627, USA
[66] State University of New York, Stony Brook, New York 11794, USA
[67] Brookhaven National Laboratory, Upton, New York 11973, USA
[68] Langston University, Langston, Oklahoma 73050, USA
[69] University of Oklahoma, Norman, Oklahoma 73019, USA
[70] Oklahoma State University, Stillwater, Oklahoma 74078, USA
[71] Brown University, Providence, Rhode Island 02912, USA
[72] University of Texas, Arlington, Texas 76019, USA
[73] Southern Methodist University, Dallas, Texas 75275, USA
[74] Rice University, Houston, Texas 77005, USA
[75] University of Virginia, Charlottesville, Virginia 22904, USA
[76] University of Washington, Seattle, Washington 98195, USA

(Dated: July 24, 2012)

We present a search for the standard model Higgs boson in 9.5 fb^{-1} of $p\bar{p}$ collisions at $\sqrt{s} = 1.96$ TeV collected with the D0 detector at the Fermilab Tevatron Collider. The final state considered contains a pair of b jets and is characterized by an imbalance in transverse energy, as expected from $p\bar{p} \to ZH \to \nu\bar{\nu}b\bar{b}$ production. The search is also sensitive to the $WH \to \ell\nu b\bar{b}$ channel when the charged lepton is not identified. The data are found to be in good agreement with the expected background. For a Higgs boson mass of 125 GeV, we set a limit at the 95% C.L. on the cross section $\sigma(p\bar{p} \to [Z/W]H)$, assuming standard model branching fractions, that is a factor of 4.3 times larger than the theoretical standard model value, while the expected factor is 3.9. The search is also used to measure a combined WZ and ZZ production cross section that is a factor of $0.94 \pm 0.31\,(\text{stat}) \pm 0.34\,(\text{syst})$ times the standard model prediction of 4.4 pb, with an observed significance of 2.0 standard deviations.

PACS numbers: 13.85.Qk, 13.85.Ni, 13.85.Rm, 14.80.Bn

INTRODUCTION

In the standard model (SM) [1], electroweak symmetry breaking is achieved via the introduction of a doublet of scalar fields, of which one degree of freedom remains once the W and Z vector bosons have acquired their masses. This degree of freedom manifests itself as a new scalar particle [2], the Higgs boson (H). Associated ZH production in $p\bar{p}$ collisions at $\sqrt{s} = 1.96$ TeV, with $Z \to \nu\bar{\nu}$ and $H \to b\bar{b}$, is among the most sensitive processes in the search for a Higgs boson with mass $M_H \lesssim 135$ GeV at the Fermilab Tevatron Collider [3]. The D0 Collaboration published a search for this process based on 5.2 fb^{-1} of integrated luminosity [4]. In this Letter, an extension of this search to the full Run II dataset is presented. The CDF Collaboration recently reported results from a similar search [5], as well as the ATLAS and CMS Collaborations using pp collisions at 7 TeV at the LHC [6, 7]. A lower limit of 114.4 GeV was set on M_H by the LEP Collaborations [8], while an upper limit at 127 GeV has been established by the ATLAS and CMS Collaborations [9, 10]. These limits and those given below are all defined at the 95% C.L. The ATLAS and CMS Collaborations have also published [9, 10] excesses above background expectations at approximately 125 GeV and have recently reported results confirming these excesses at the five standard deviations level [11, 12].

The final-state topology considered in this search consists of a pair of b jets from $H \to b\bar{b}$ decay and missing

*with visitors from [a]Augustana College, Sioux Falls, SD, USA, [b]The University of Liverpool, Liverpool, UK, [c]UPIITA-IPN, Mexico City, Mexico, [d]DESY, Hamburg, Germany, [e]SLAC, Menlo Park, CA, USA, [f]University College London, London, UK, [g]Centro de Investigacion en Computacion - IPN, Mexico City, Mexico, [h]ECFM, Universidad Autonoma de Sinaloa, Culiacán, Mexico and [i]Universidade Estadual Paulista, São Paulo, Brazil.

transverse energy ($\not\!\!E_T$) from $Z \to \nu\bar{\nu}$. The search is also sensitive to the WH process when the charged lepton from $W \to \ell\nu$ decay is not identified. The main backgrounds arise from (W/Z)+heavy-flavor jets (jets initiated by b or c quarks), top quark production, and multijet (MJ) events with $\not\!\!E_T$ arising from mismeasurement of jet energies. A boosted-decision-tree discriminant based on kinematic properties is first used to reject most of the multijet events. Next, jets from candidate Higgs boson decays are required to be identified as b jets. Finally, discrimination between signal and remaining backgrounds is achieved by means of additional boosted decision trees.

To validate the techniques used in the search for the Higgs boson, the analysis is also interpreted as a measurement of WZ and ZZ diboson production. The only modification is in the training of the final discriminants, for which a diboson signal is used instead of a Higgs boson signal.

DATA AND SIMULATED SAMPLES

The D0 detector used for Tevatron Run II (2001 – 2011) is described in detail in Ref. [13]. Its main components are: a tracking system surrounding the beam pipe, followed by a liquid-argon and uranium sampling calorimeter, and then a muon system. The tracking system is immersed in a 2 T magnetic field provided by a superconducting solenoid and consists of a silicon microstrip tracker followed by a scintillating fiber tracker. The calorimeter is composed of a central and two end sections housed in separate cryostats. Each section is segmented in depth, with four electromagnetic layers followed by up to five hadronic layers. Scintillating tiles provide additional sampling between the cryostats. The muon system consists of tracking and trigger detectors in front of and beyond 1.8 T iron toroids. Online event selection is provided by a three-level trigger system.

The data used in this analysis were recorded using triggers designed to select events with jets and $\not\!\!E_T$ [14]. After imposing data quality requirements, the total integrated luminosity recorded with these triggers is 9.5 fb^{-1}, corresponding to all available Run II data for this analysis.

The analysis relies on (i) charged particle tracks, (ii) calorimeter jets reconstructed in a cone of radius 0.5 in y-ϕ space, where y is the rapidity and ϕ the azimuthal angle, using the iterative midpoint cone algorithm [15], and (iii) electrons or muons identified through the association of tracks with electromagnetic calorimeter clusters or with hits in the muon detector, respectively. The $\not\!\!E_T$ is reconstructed as the negative of the vectorial sum of the transverse components of energy deposits in the calorimeter and is corrected for identified muons. Jet energies are calibrated using primarily transverse energy balance in photon+jet events [16], and these corrections are propagated to the $\not\!\!E_T$ assessment.

Those backgrounds arising from MJ processes with instrumental effects giving rise to $\not\!\!E_T$ are estimated from data. The remainder of the backgrounds and the signal processes are simulated by Monte Carlo (MC). Events from (W/Z)+jets processes are generated with ALPGEN [17], interfaced with PYTHIA [18] for initial- and final-state radiation and for hadronization. The p_T spectrum of the Z boson is reweighted to match the D0 measurement [19]. The p_T spectrum of the W boson is reweighted using the same experimental input, corrected for the differences between the W and Z p_T spectra predicted in next-to-next-to-leading order (NNLO) QCD [20]. To simulate $t\bar{t}$ and electroweak single top quark production, the ALPGEN and SINGLETOP [21] generators, respectively, are interfaced with PYTHIA, while vector boson pair production is generated with PYTHIA. The ZH and WH signal processes are generated with PYTHIA for Higgs boson masses from 100 to 150 GeV in 5 GeV steps. All these simulations use CTEQ6L1 parton distribution functions (PDFs) [22].

The absolute normalizations for (W/Z) inclusive production are obtained from NNLO calculations of total cross sections [23] using the MSTW2008 NNLO PDFs [24]. The heavy-flavor fractions in (W/Z)+jets are obtained using MCFM [25] at next-to-leading order (NLO). The diboson cross sections are also calculated with MCFM [27]. Cross sections for pair and single top quark production are taken from Ref. [26]. For signal processes, cross sections are taken from Ref. [28].

Signal and background samples are passed through a full GEANT3-based simulation [29] of the detector response and processed with the same reconstruction program as used for data. Events from randomly selected beam crossings with the same instantaneous luminosity distribution as data are overlaid on simulated events to account for detector noise and contributions from additional $p\bar{p}$ interactions. Parameterizations of the trigger efficiencies are determined using events collected with independent triggers based on information from the muon detectors. Corrections for residual differences between data and simulation are applied for electron, muon, and jet identification. Jet energy calibration and resolution are adjusted in simulated events to match those measured in data.

EVENT SELECTION

A preselection that greatly reduces the overwhelming background from multijet events is performed as follows. The interaction vertex must be reconstructed within the acceptance of the silicon vertex detector and at least three tracks must originate from that vertex. Jets with associated tracks that meet criteria ensuring that the b-tagging algorithm operates efficiently are denoted as "taggable" jets, except for those also identified

as hadronic decays of τ leptons [30]. Exactly two taggable jets are required, one of which must be the leading (highest p_T) jet in the event; the Higgs candidate is formed from these two jets, denoted jet_1 and jet_2 (ordered in decreasing p_T). These jets must have transverse momentum $p_T > 20$ GeV and pseudorapidity $|\eta| < 2.5$. The two taggable jets must not be back-to-back in the plane transverse to the beam direction: $\Delta\phi(\text{jet}_1, \text{jet}_2) < 165°$. Finally, $\not\!\!E_T > 40$ GeV is required.

Additional selection criteria define four distinct samples: (i) an "analysis" sample used to search for a Higgs boson signal; (ii) an "electroweak (EW) control" sample used to validate the background MC simulation, enriched in $W(\to \mu\nu)$+jets events where the jet system has a topology similar to that of the analysis sample; (iii) an "MJ-model" sample, dominated by multijet events, used to model the MJ background in the analysis sample; and (iv) a large "MJ-enriched" sample, used to validate this MJ-modeling procedure.

The analysis sample is selected by requiring the scalar sum of the transverse momenta of the two leading taggable jets to be greater than 80 GeV and a measure of the $\not\!\!E_T$ significance $\mathcal{S} > 5$ [31]. Larger values of $\mathcal{S}$ correspond to $\not\!\!E_T$ values that are less likely to be caused by fluctuations in jet energies. The $\mathcal{S}$ distribution is shown for the analysis sample in Fig. 9.

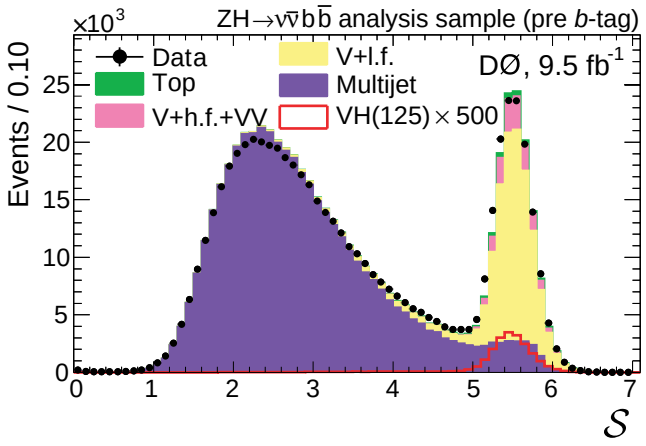

FIG. 1: (Color online.) The measure $\mathcal{S}$ of $\not\!\!E_T$ significance in the analysis sample without the requirement that $\mathcal{S}$ be larger than 5. The data are shown as points with error bars and the background contributions as histograms: dibosons are labeled as "VV," "V+l.f." includes (W/Z)+(u, d, s, g) jets, "V+h.f." includes (W/Z)+(b, c) jets, and "Top" includes pair and single top quark production. The distribution for signal (VH) is scaled by a factor of 500 and includes ZH and WH production for $M_H = 125$ GeV.

The dominant signal topology is a pair of b jets recoiling against the $\not\!\!E_T$ due to the neutrinos from $Z \to \nu\bar{\nu}$ decay, leading to the direction of the $\not\!\!E_T$ being at a large angle with respect to the direction of each jet. In contrast, in events from MJ background with fluctuations in jet energy measurement, the $\not\!\!E_T$ tends to be aligned with a mismeasured jet. A second estimate of the $\not\!\!E_T$ can be obtained from the missing p_T, $\not\!\!p_T$, calculated from the reconstructed charged particle tracks originating from the interaction vertex. This variable is less sensitive to jet energy measurement fluctuations. In signal events, $\not\!\!p_T$ is also expected to point away from both jets, while for MJ background, its angular distribution is expected to be more isotropic. Advantage is taken of these features through the variable $\mathcal{D} = [\Delta\phi(\not\!\!p_T, \text{jet}_1) + \Delta\phi(\not\!\!p_T, \text{jet}_2)]/2$. For signal events, as well as for the non-MJ backgrounds, $\mathcal{D} > \pi/2$ in the vast majority of events, whereas the MJ background events tend to be symmetrically distributed around $\pi/2$. In the analysis sample, $\mathcal{D} > \pi/2$ is therefore required. To improve the efficiency of this criterion for the $(W \to \mu\nu)H$ signal with non-identified muons, tracks satisfying isolation criteria are removed from the $\not\!\!p_T$ computation. The reverse of the $\mathcal{D}$ requirement is also used to define the MJ-model sample, as explained below.

Events containing an isolated electron or muon with $p_T > 15$ GeV are rejected to ensure there is no overlap with the D0 WH search in the lepton+$\not\!\!E_T$ topology [32].

The EW control sample is selected in a similar manner to the analysis sample, except that an isolated muon with $p_T > 15$ GeV is required. The multijet content of this sample is rendered negligible by requiring that the transverse mass of the muon and $\not\!\!E_T$ system is larger than 30 GeV and that the $\not\!\!E_T$, calculated taking account of the muon from the W boson decay, is greater than 20 GeV. To ensure similar jet topologies for the analysis and EW control samples, the $\not\!\!E_T$, not corrected for the selected muon, is required to exceed 40 GeV. The number of selected events is in good agreement with the SM expectation. All the kinematic distributions are also well described once reweightings of the distributions of $\Delta\eta(\text{jet}_1, \text{jet}_2)$ and $\eta(\text{jet}_2)$ are performed, as suggested by a comparison [33] of data with a simulation of (W/Z)+jets using the SHERPA generator [34]. The distribution of the dijet mass in the EW control sample is shown in Fig. 11(a).

The MJ-model sample, used to determine the MJ background, is selected in the same manner as the analysis sample, except that the requirement $\mathcal{D} > \pi/2$ is reversed. The small remaining contributions from non-MJ SM background processes in the $\mathcal{D} < \pi/2$ region are subtracted, and the resulting sample is used to model the MJ background in the analysis sample. The MJ background in the region $\mathcal{D} > \pi/2$ is normalized by performing a fit of the sum of the MJ and SM backgrounds to the $\not\!\!E_T$ distribution of the data in the analysis sample.

The MJ-enriched sample is used to test the validity of this approach and is defined in the same manner as the analysis sample, except that $\mathcal{S} < 4.5$ is now required (see Fig. 9). As a result, the MJ background dominates the entire range of $\mathcal{D}$ values, and this sample is used to verify that the events with $\mathcal{D} < \pi/2$ correctly model those with

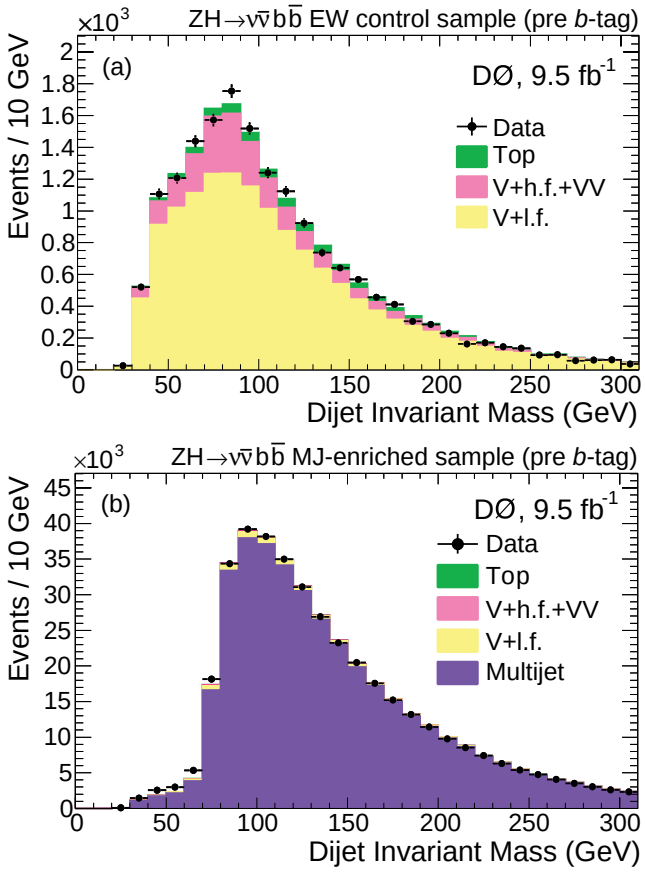

FIG. 2: (Color online.) Distributions of the dijet mass before b-tagging in the (a) EW control and (b) MJ-enriched samples. The data are shown as points with error bars and the background contributions as histograms: dibosons are labeled as "VV," "V+l.f." includes (W/Z)+(u, d, s, g) jets, "V+h.f." includes (W/Z)+(b, c) jets, and "Top" includes pair and single top quark production.

$\mathcal{D} > \pi/2$. The distribution of the dijet mass in the MJ-enriched sample is shown in Fig. 11(b).

A multivariate b-tagging discriminant, with several boosted decision trees as inputs, is used to select events with one or more b quark candidates. This algorithm is an upgraded version of the neural network b-tagging technique described in Ref. [35]. The new algorithm includes more information related to the lifetime of the jet and results in a better discrimination between b and light (u, d, s, g) jets. It provides an output between 0 and 1 for each jet, with a value closer to one indicating a higher probability that the jet originated from a b quark. The output from the algorithm measured in simulated events is adjusted to match the output measured in dedicated data samples as described in more detail in Ref. [35]. ¿From this continuous output, thirteen operating points $(L_b = 0, 1, \ldots, 12)$ are defined, with b purity increasing with L_b. Jets with $L_b = 0$ are defined as untagged. The typical per-b-jet efficiency and misidentification rate for light-flavor jets are about 80% (50%) and 10% (1%) for the loosest non-zero (tightest) b-tag operating point, respectively.

To improve the sensitivity of the analysis, two high signal purity samples are defined from the analysis sample using the variable $L_{bb} = L_b(\text{jet}_1) + L_b(\text{jet}_2)$. The two samples are defined as follows: a tight b-tag sample with $L_{bb} \geq 18$ and a medium b-tag sample with $11 \leq L_{bb} \leq 17$. The medium b-tag sample contains events with two loosely b-tagged jets, as well as events with one tightly b-tagged jet and one untagged jet. The signal-to-background ratios for a Higgs boson mass of 125 GeV in the pre, medium, and tight b-tag samples, after applying a multijet veto (defined in the next section), are respectively 0.035%, 0.23%, and 1.00%.

ANALYSIS USING DECISION TREES

A stochastic gradient boosted decision tree (DT) technique is employed, as implemented in the TMVA package [36], to improve the discrimination between signal and background processes.

First, an "MJ DT" (multijet-rejection DT) is trained to discriminate between signal and MJ-model events before b-tagging is applied. To avoid Higgs boson mass dependence at this stage of the analysis, signal events are not used, and the MJ DT is trained on a sample of (W/Z)+heavy-flavor jets events instead. Variables that provide some discrimination have been chosen for the MJ DT, excluding those strongly correlated to the Higgs mass (such as the dijet mass itself or the $\Delta R = \sqrt{(\Delta\eta)^2 + (\Delta\phi)^2}$ between jet_1 and jet_2).

The MJ DT output, which ranges between -1 and $+1$, is shown in Fig. 13 for the analysis sample after the medium b-tagging requirement. Good agreement is seen between data and the predicted background. A value of the multijet discriminant in excess of -0.3 is required (multijet veto), which removes 93% of the multijet background while retaining 90% of the signal for $M_H = 125$ GeV. The numbers of expected signal and background events, as well as the number of observed events, are given in Table I after imposing the multijet veto. Dijet mass distributions in the analysis sample after the multijet veto are shown in Fig. 4 for b-tagged events.

Next, to separate signal from the remaining SM backgrounds, two "SM DTs" (SM-background-rejection DTs) are trained for each M_H, one in the medium b-tag channel and one in the tight b-tag channel. Some of the MJ DT input variables are used again, but most of the discrimination comes from additional kinematic variables correlated to the Higgs boson mass, of which, as expected, the dijet mass has the strongest discriminating power. The SM DT outputs, which range between -1 and $+1$, are used as final discriminants. Their distributions are

TABLE I: The numbers of expected signal, expected background, and observed data events after the multijet veto, for the pre, medium, and tight b-tag samples. The signal corresponds to $M_H = 125$ GeV, "Top" includes pair and single top quark production, and "VV" is the sum of all diboson processes. The uncertainties quoted on the signal and total background arise from the statistics of the simulation and from the sources of systematic uncertainties mentioned in the text.

Sample	ZH	WH	W+jets	Z+jets	Top	VV	MJ	Total Background	Observed
Pre b-tag	18.3 ± 1.8	16.7 ± 1.6	66895	25585	1934	3144	1977	99535 ± 12542	98980
Medium b-tag	6.7 ± 0.7	6.1 ± 0.6	3112	1074	761	237	278	5462 ± 776	5453
Tight b-tag	6.0 ± 0.8	5.3 ± 0.7	443	252	377	56	6	1134 ± 192	1039

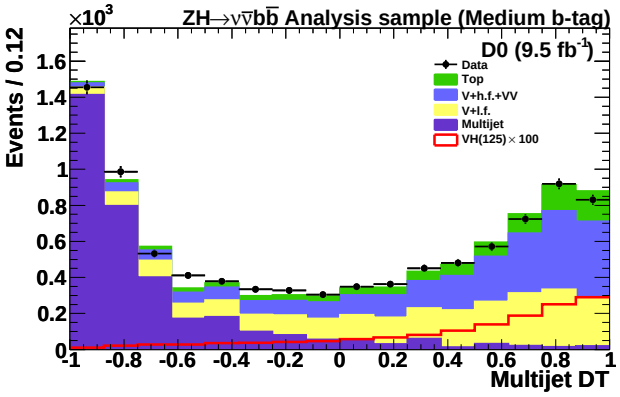

FIG. 3: (Color online.) Distribution of the MJ DT output after the medium b-tagging requirement in the analysis sample. The distribution for signal (VH), shown for $M_H = 125$ GeV, is scaled by a factor of 100 and includes ZH and WH production. The data are shown as points with error bars and the background contributions as histograms: dibosons are labeled as "VV," "V+l.f." includes $(W/Z)+(u, d, s, g)$ jets, "V+h.f." includes $(W/Z)+(b, c)$ jets, and "Top" includes pair and single top quark production.

shown in Fig. 5 for $M_H = 125$ GeV.

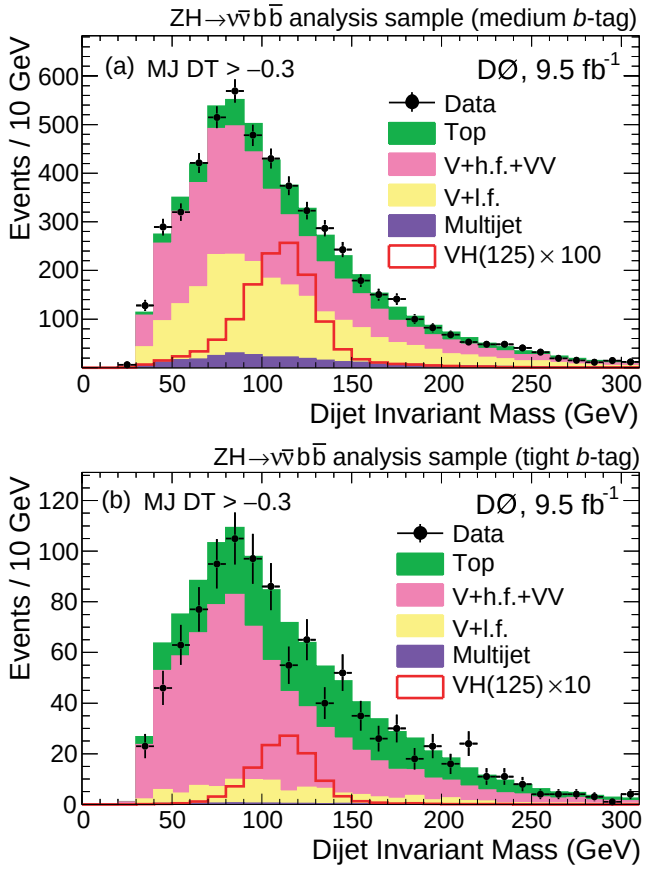

FIG. 4: (Color online.) Dijet invariant mass in the analysis sample after the multijet veto for events with (a) medium b-tag and (b) tight b-tag. The distributions for signal (VH), which are scaled by a factor of 100 for medium b-tag and 10 for tight b-tag respectively, include ZH and WH production for $M_H = 125$ GeV. The data are shown as points with error bars and the background contributions as histograms: dibosons are labeled as "VV," "V+l.f." includes $(W/Z)+(u, d, s, g)$ jets, "V+h.f." includes $(W/Z)+(b, c)$ jets, and "Top" includes pair and single top quark production.

SYSTEMATIC UNCERTAINTIES

Experimental uncertainties arise from the integrated luminosity (6%) [37], the trigger simulation (2%), the jet energy calibration and resolution [(1–2)%], jet reconstruction and taggability (3%), the lepton identification (1%), the modeling of the MJ background (25%, which translates into a 1% uncertainty on the total background), and the b-tagging (from 4% for background in the medium b-tag sample to 9% for signal in the tight b-tag sample). In addition to the impact of these uncertainties on the integrated signal and background yields mentioned above, modifications of the shapes of the final discriminants are also considered, when relevant. Correlations among systematic uncertainties in signal and each background are taken into account when extracting the final results.

Theoretical uncertainties on cross sections for SM processes are estimated as follows. For (W/Z)+jets production, an uncertainty of 10% is assigned to the total cross sections and an uncertainty of 20% to the heavy-flavor fractions (estimated using MCFM at NLO [25]). For other SM backgrounds, uncertainties are taken from Ref. [26] or using MCFM [27] and range from 6% to 10%. The uncertainties on cross sections for signal (7%) are taken from Ref. [28]. Uncertainties on the shapes of the final

discriminants arise from (i) the modeling of (W/Z)+jets, assessed by varying the renormalization and factorization scales and by comparing results from ALPGEN interfaced with HERWIG [38] to ALPGEN interfaced with PYTHIA, and (ii) the choice of PDFs, estimated using the prescription of Ref. [22].

LIMIT SETTING PROCEDURE

Agreement is found between data and the predicted background, both in the numbers of selected events (Table I) and in the distributions of final discriminants (Fig. 5), once systematic uncertainties are taken into account. The modified frequentist CL_s approach [39] is used to set limits on the cross section for SM Higgs boson production, where the test statistic is a log-likelihood ratio (LLR) for the background-only and signal+background hypotheses. The result is obtained by summing LLR values over the bins in the final discriminants shown in Fig. 5. The impact of systematic uncertainties on the sensitivity of the analysis is reduced by maximizing a "profile" likelihood function [40] in which these uncertainties are given Gaussian constraints associated with their priors. Figure 15 shows a comparison of the SM DT distributions expected for a signal with $M_H = 125$ GeV and observed for the background-subtracted data. The subtracted background and its uncertainties are the result of the profile likelihood fit to the data under the background-only hypothesis.

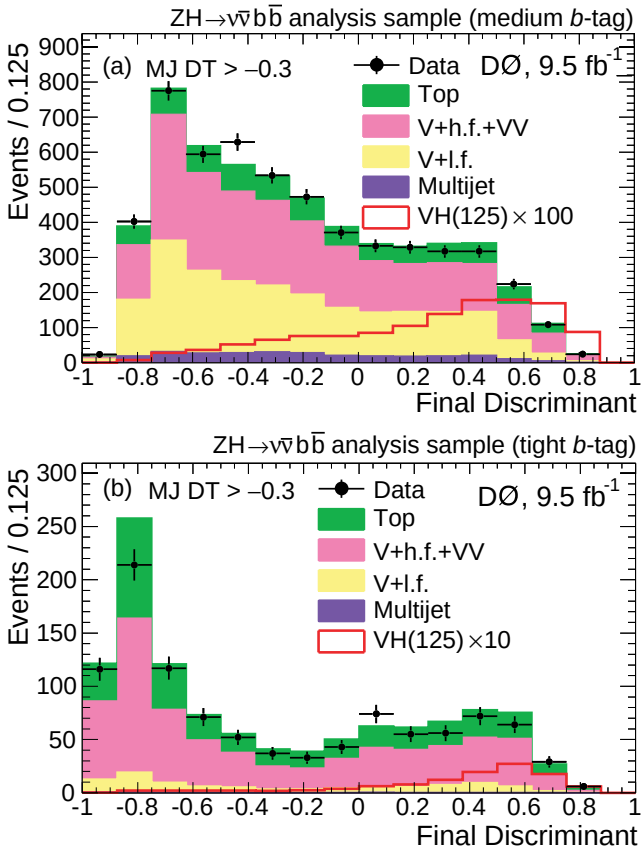

FIG. 5: (Color online.) The SM DT output for the $(W/Z)H$ search with $M_H = 125$ GeV following the multijet veto for events with (a) medium b-tag and (b) tight b-tag prior to the fit to data. The distributions for signal (VH) are scaled by a factor of 100 for medium b-tag events and 10 for tight b-tag events, respectively, and include ZH and WH production for $M_H = 125$ GeV. The data are shown as points with error bars and the background contributions as histograms: dibosons are labeled as "VV," "V+l.f." includes (W/Z)+(u, d, s, g) jets, "V+h.f." includes (W/Z)+(b, c) jets, and "Top" includes pair and single top quark production.

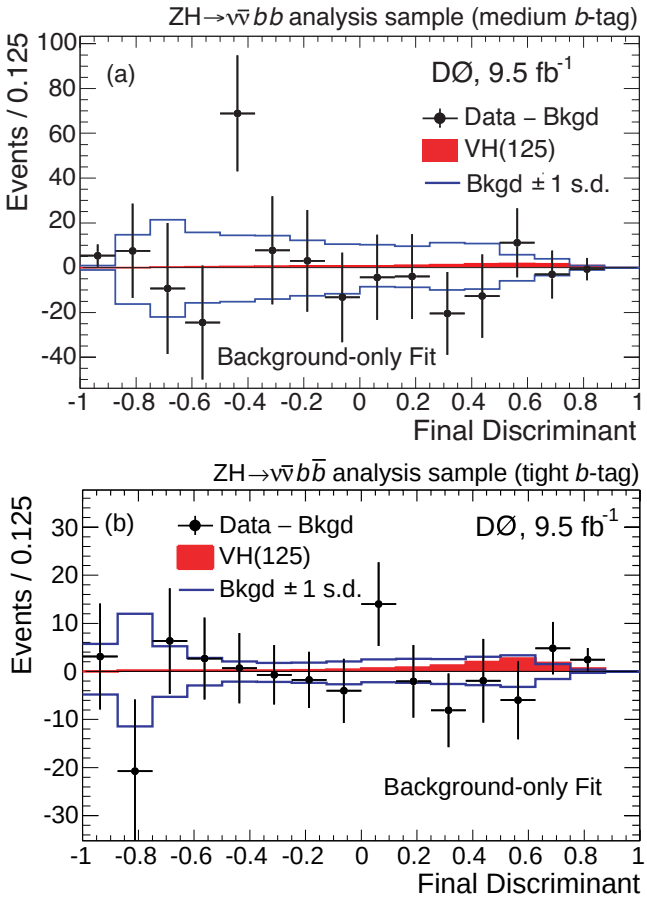

FIG. 6: (Color online.) Final discriminant distributions expected for a SM VH signal with $M_H = 125$ GeV (filled histogram) and observed for background-subtracted data (points with statistical error bars) for the (a) medium and (b) tight b-tag channels. The subtracted background is the result of the profile likelihood fit to the data under the background-only hypothesis. Also shown is the ±1 standard deviation (s.d.) band on the fitted background. No scaling factor is applied to the signal.

HIGGS BOSON SEARCH RESULTS

The results are given as limits in Table II and Fig. 7(a) and in terms of LLR values in Fig. 7(b). For $M_H = 125$ GeV, the observed and expected limits on the combined cross section of ZH and WH production are factors of 4.3 and 3.9 larger than the SM value, respectively, assuming SM branching fractions. In Fig. 7(b), the median expected LLR in the presence of a Higgs boson with a mass of 125 GeV is also shown for comparison.

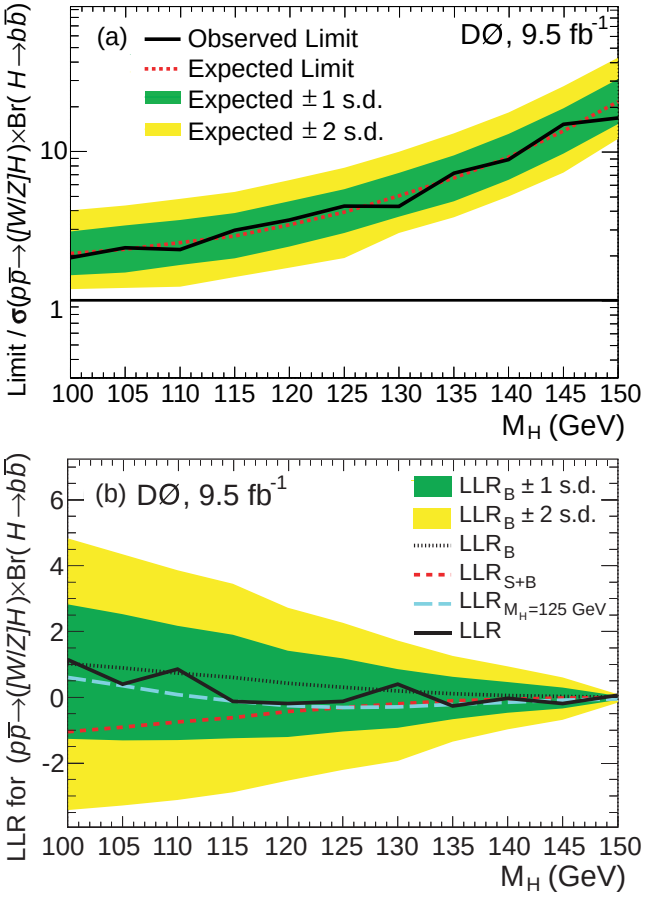

FIG. 7: (Color online.) (a) Ratio of the observed (solid black) and expected (dotted red) exclusion limits to the SM production cross section. (b) The observed (solid black) and expected LLRs for the background-only (black dots) and signal+background hypotheses (short red dashes), as well as the LLR expected in the presence of a Higgs boson with $M_H = 125$ GeV (long blue dashes). All are shown as a function of the tested value of M_H with the green and yellow shaded areas corresponding to the 1 and 2 standard deviation (s.d.) variations around the background-only hypothesis.

DIBOSON SEARCH RESULTS

The final states arising from the SM production of $(Z \to \nu\bar{\nu})(Z \to b\bar{b})$ and $(W \to \ell\nu)(Z \to b\bar{b})$ are the same in particle content and topology as those used for the Higgs boson search reported above when the lepton from $W \to \ell\nu$ is not reconstructed. Evidence for ZZ and WZ production can therefore be used to validate the techniques employed in the Higgs boson search. The only modification to the analysis is in the training of the final discriminants, where ZZ and WZ are now treated as signal with the remaining diboson process, WW, kept as background. A cross section scale factor of $0.94 \pm 0.31\,(\text{stat}) \pm 0.34\,(\text{syst})$ is measured with respect to the predicted SM value of (4.4 ± 0.3) pb [27], with an observed (expected) significance of 2.0 (2.1) standard deviations.

The measurement of the diboson cross section has also been carried out using as final discriminants the distributions of dijet invariant mass (as opposed to the SM DTs) in the medium and tight b-tag samples. A cross section scale factor of $1.08 \pm 0.35\,(\text{stat}) \pm 0.39\,(\text{syst})$ is measured with respect to the predicted SM value, with an observed (expected) significance of 2.0 (1.9) standard deviations. The expected significance is slightly lower than the one expected with the multivariate analysis, in which additional discrimination is provided by variables such as the angular separation between jets or the event centrality.

Figure 17 shows the final discriminant distributions in the medium and tight b-tag channels, as well as the dijet mass distribution summed over the medium and tight b-tag channels, for the expected $WZ + ZZ$ signal and for the background-subtracted data. The subtracted backgrounds and their uncertainties are the results of the profile likelihood fits to the data under the signal+background hypothesis.

SUMMARY

We have performed a search for the standard model Higgs boson in 9.5 fb^{-1} of $p\bar{p}$ collisions at $\sqrt{s} = 1.96$ TeV collected with the D0 detector at the Fermilab Tevatron Collider. The final state considered contains a pair of b jets and is characterized by an imbalance in transverse energy, as expected from $p\bar{p} \to ZH \to \nu\bar{\nu}b\bar{b}$ production and decays. The search is also sensitive to the $WH \to \ell\nu b\bar{b}$ channel when the charged lepton is not identified. The data are found to be in good agreement with the expected background. For a Higgs boson mass of 125 GeV, we set a limit at the 95% C.L. on the cross section $\sigma(p\bar{p} \to [Z/W]H)$, assuming standard model branching fractions, that is a factor of 4.3 larger than the theoretical standard model value, for an expected factor of 3.9.

To validate our analysis techniques, we also performed a search for WZ and ZZ production, resulting in a measurement of the combined cross section that is a factor of $0.94 \pm 0.31\,(\text{stat}) \pm 0.34\,(\text{syst})$ relative to the standard model prediction, with a significance of 2.0 standard de-

TABLE II: The expected and observed upper limits measured using 9.5 fb^{-1} of integrated luminosity on the ZH plus WH production cross section relative to the SM expectation, assuming SM branching fractions, as a function of M_H.

m_H (GeV)	100	105	110	115	120	125	130	135	140	145	150
Expected	2.1	2.2	2.4	2.7	3.2	3.9	5.0	6.7	9.2	13.8	21.6
Observed	1.9	2.3	2.2	3.0	3.5	4.3	4.3	7.2	8.8	15.3	16.8

viations.

ACKNOWLEDGEMENTS

We thank the staffs at Fermilab and collaborating institutions, and acknowledge support from the DOE and NSF (USA); CEA and CNRS/IN2P3 (France); MON, NRC KI and RFBR (Russia); CNPq, FAPERJ, FAPESP and FUNDUNESP (Brazil); DAE and DST (India); Colciencias (Colombia); CONACyT (Mexico); NRF (Korea); FOM (The Netherlands); STFC and the Royal Society (United Kingdom); MSMT and GACR (Czech Republic); BMBF and DFG (Germany); SFI (Ireland); The Swedish Research Council (Sweden); and CAS and CNSF (China).

[1] S. L. Glashow, Nucl. Phys. **B22**, 579 (1961); S. Weinberg, Phys. Rev. Lett. **19**, 1264 (1967); A. Salam, Proc. 8th Nobel Symposium, Stockholm 1968 (Almqvist and Wiksells, Stockholm, 1968).
[2] F. Englert and R. Brout, Phys. Rev. Lett. **13**, 321 (1964); P. W. Higgs, Phys. Rev. Lett. **13**, 508 (1964); G. S. Guralnik, C. R. Hagen, and T. W. B. Kibble, Phys. Rev. Lett. **13**, 585 (1964).
[3] M. Carena *et al.*, `arXiv:hep-ph/0010338`.
[4] V. M. Abazov *et al.* (D0 Collaboration), Phys. Rev. Lett. **104**, 071801 (2010).
[5] T. Aaltonen *et al.* (CDF Collaboration), to be published in Phys. Rev. Lett., arXiv:1207.1711.
[6] S. Chatrchyan *et al.* (CMS Collaboration), Phys. Lett. B **710**, 284 (2012).
[7] G. Aad *et al.* (ATLAS Collaboration), to be published in Phys. Lett. B, arXiv:1207.0210.
[8] R. Barate *et al.* (LEP Working Group for Higgs boson searches), Phys. Lett. B **565**, 61 (2003).
[9] S. Chatrchyan *et al.* (CMS Collaboration), Phys. Lett. B **710**, 26 (2012).
[10] G. Aad *et al.* (ATLAS Collaboration), Phys. Rev. D **86**, 032003 (2012).
[11] G. Aad *et al.* (ATLAS Collaboration), to be published in Phys. Lett. B, arXiv:1207.7214.
[12] S. Chatrchyan *et al.* (CMS Collaboration), to be published in Phys. Lett. B, arXiv:1207.7235.
[13] V. M. Abazov *et al.* (D0 Collaboration), Nucl. Instrum. Methods Phys. Res. A **565**, 463 (2006); S. Abachi *et al.* (D0 Collaboration), Nucl. Instrum. Methods Phys. Res. A **338**, 185 (1994); M. Abolins *et al.*, Nucl. Instrum. Methods Phys. Res. A **584**, 75 (2008); R. Angstadt *et al.*, Nucl. Instrum. Methods Phys. Res. A **622**, 298 (2010).
[14] C. Ochando, FERMILAB-THESIS-2008-78.
[15] G. C. Blazey *et al.*, `arXiv:hep-ex/0005012`.
[16] V. M. Abazov *et al.* (D0 Collaboration), Phys. Rev. D **85**, 052006 (2012).
[17] M. L. Mangano *et al.*, J. High Energy Phys. **07**, 001 (2003); we use version 2.11.
[18] T. Sjöstrand, S. Mrenna, and P. Skands, J. High Energy Phys. **05**, 026 (2006); we use version 6.409, D0 Tune A.
[19] V. M. Abazov *et al.* (D0 Collaboration), Phys. Rev. Lett. **100**, 102002 (2008).
[20] K. Melnikov and F. Petriello, Phys. Rev. D **74**, 114017 (2006).
[21] E. Boos *et al.*, Nucl. Instrum. Methods Phys. Res. A **534**, 250 (2004); E. Boos *et al.*, Phys. Atom. Nucl. **69**, 1317 (2006).
[22] J. Pumplin *et al.*, J. High Energy Phys. **07**, 012 (2002); D. Stump *et al.*, J. High Energy Phys. **10**, 046, (2003).
[23] R. Hamberg, W. L. van Neerven, and T. Matsuura, Nucl. Phys. **B359**, 343 (1991); ibid, **B644**, 403 (2002).
[24] A. D. Martin, W. J. Stirling, R. S. Thorne, and G. Watt, Eur. Phys. J. C **63**, 189 (2009).
[25] R. K. Ellis and S. Veseli, Phys. Rev. D **60**, 011501 (1999); J. M. Campbell and R. K. Ellis, Phys. Rev. D **62**, 114012 (2000); updated using J. Campbell, K. Ellis, and C. Williams, MCFM – Monte Carlo for FeMtobarn processes, `http://mcfm.fnal.gov/`.
[26] U. Langenfeld, S. Moch, and P. Uwer, Phys. Rev. D **80**, 054009 (2009); N. Kidonakis, Phys. Rev. D **74**, 114012 (2006).
[27] J. M. Campbell and R. K. Ellis, Phys. Rev. D **60**, 113006 (1999); updated using J. Campbell, K. Ellis, and C. Williams, MCFM – Monte Carlo for FeMtobarn processes, `http://mcfm.fnal.gov/`.
[28] J. Baglio and A. Djouadi, J. High Energy Phys. **10**, 064 (2010).
[29] R. Brun and F. Carminati, CERN Program Library Long Writeup W5013, 1993 (unpublished).
[30] V. M. Abazov *et al.* (D0 Collaboration), Phys. Lett. B **670**, 292 (2009).
[31] A. Schwartzman, FERMILAB-THESIS-2004-21.
[32] V. M. Abazov *et al.* (D0 Collaboration), Phys. Rev. D **86**, 032005 (2012).
[33] V. M. Abazov *et al.* (D0 Collaboration), Phys. Lett. B **669**, 278 (2008).
[34] T. Gleisberg *et al.*, J. High Energy Phys. **02**, 056 (2004); J. Alwall *et al.*, Eur. Phys. J. C **53**, 473 (2008).
[35] V. M. Abazov *et al.* (D0 Collaboration), Nucl. Instrum. Methods Phys. Res. A **620**, 490 (2010).
[36] H. Voss *et. al.*, PoS (**ACAT**), 040 (2007), arXiv:physics/0703039; we use version 4.1.0.
[37] T. Andeen *et al.*, FERMILAB-TM-2365, 2007.
[38] G. Corcella *et al.*, J. High Energy Phys. **01**, 010 (2001).

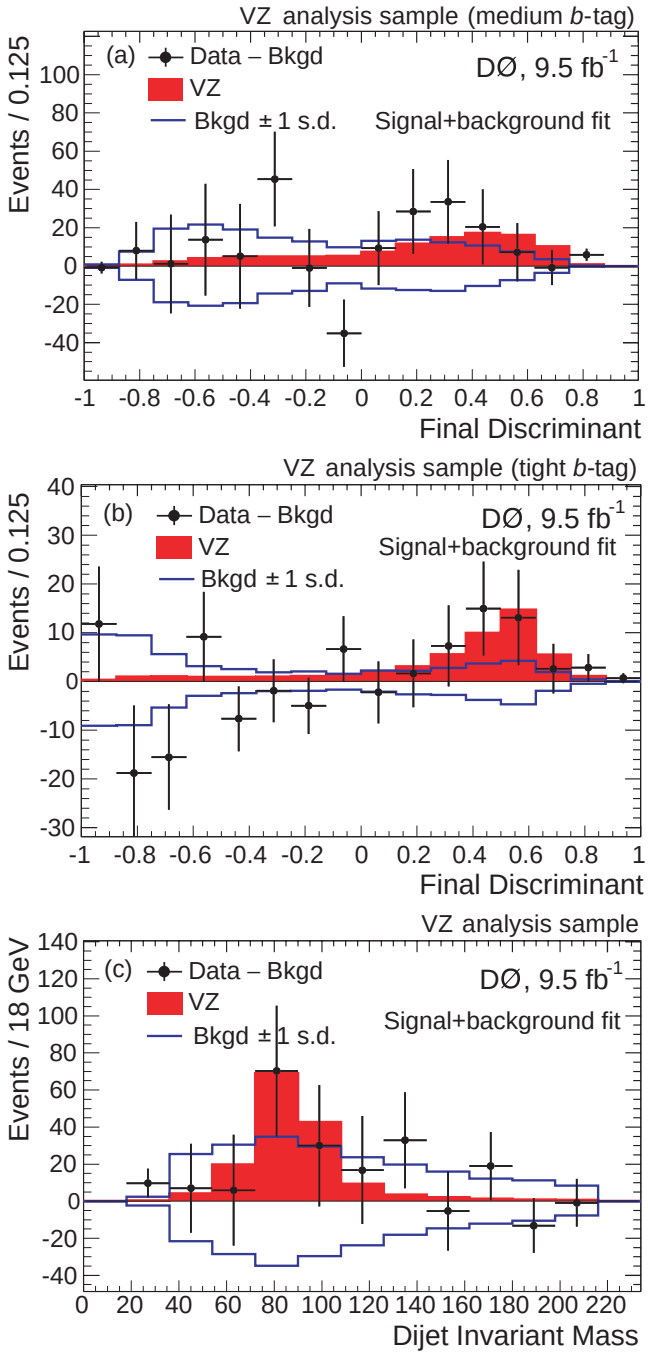

FIG. 8: (Color online.) Final discriminant distributions expected for a WZ plus ZZ signal (filled histogram) and observed for background-subtracted data (points with statistical error bars) for the (a) medium and (b) tight b-tag channels. (c) Similarly for the dijet mass distribution, summed over the medium and tight b-tag channels. The subtracted backgrounds are the results of profile likelihood fits to the data under the signal+background hypothesis. Also shown are the ± 1 standard deviation (s.d.) bands on the fitted backgrounds. The signal is scaled to the SM cross section.

[39] T. Junk, Nucl. Instrum. Methods Phys. Res. A **434**, 435 (1999); A. Read, J. Phys. G **28**, 2693 (2002).
[40] W. Fisher, FERMILAB-TM-2386-E, 2006.

Supplementary material

Introduction

No added material.

Data and Simulated Samples

No added material.

Event selection

The $\mathcal{S}$ distribution is shown for the analysis and EW-control samples in Fig. 9.

The effectiveness of the use of the variable $\mathcal{D} = (\Delta\phi(\not{p}_T, \text{jet}_1) + \Delta\phi(\not{p}_T, \text{jet}_2))/2$ can be seen in Fig. 10, where the distribution of $\mathcal{D}$ is shown for the EW control sample, dominated by events with real $\not{E}_T$, and for the MJ-enriched sample, dominated by events with $\not{E}_T$ arising from instrumental effects. For signal events, as well as for the non-MJ backgrounds, it is expected that $\mathcal{D} > \pi/2$ in the vast majority of events, whereas the MJ background events tend to be symmetrically distributed around $\pi/2$. In the analysis sample, $\mathcal{D} > \pi/2$ is therefore required.

The distributions for the pre b-tag sample dijet ΔR and $\not{H}_T/H_T$ (defined in Table III), and for the dijet invariant mass for medium b-tag and tight b-tag samples are shown in Fig. 11 for the EW-control sample and in Fig. 12 for the MJ-enriched sample.

Analysis using decision trees

The full list of the seventeen input variables to the MJ DT is given in Table III.

The MJ DT output is shown for the analysis and EW control samples after the medium b tagging requirement in Fig. 13.

The distributions for the dijet invariant mass, missing E_T, dijet ΔR and the b-tagging discriminating variable (L_{bb}) are shown in Fig. 14 for the analysis sample after the multijet veto and before any b-tagging requirement.

The full list of variables used in the SM DT is shown in Table III.

Systematic uncertainties

Systematic uncertainties are summarized in Table IV. The numbers quoted are uncertainties on total yields. The background cross sections entry represents the global effect of cross section uncertainties on the sum of backgrounds. There is no luminosity uncertainty associated with the multijet normalization since it comes from real data. The multijet is a non-negligible background component in medium b-tag sample.

In addition to the impact of these uncertainties on the integrated signal and background yields, modifications of the shapes of the final discriminants are also considered, when relevant. These originate mainly from jet corrections (energy scale, resolution and b-tagging) and also have small contributions from Monte Carlo reweightings and from parton distribution function variations.

Limit setting procedure

Figure 15 shows for $m_H = 125$ GeV the SM DT distributions after profiling. In this case, the background prediction and its uncertainties have been determined from the fit to data under the background-only hypothesis.

Higgs Search Results

No added material.

Diboson Search Results

The medium and tight b-tag SM DTs are shown in Fig. 16.

Figure 17 shows the SM DT distributions. The background prediction and its uncertainties have been determined from a fit to the data under the signal+background hypothesis.

Figure 18 shows the dijet invariant mass distributions, along with the background-subtracted data. The background prediction and its uncertainties have been determined from a fit to the data under the signal+background hypothesis.

Summary

No added material.

TABLE III: Variables used as input to the decision trees, where the angles θ and ϕ are the polar and azimuthal angles defined with respect to the proton beam direction. jet_1 refers to the leading taggable jet, jet_2 refers to the next-to-leading taggable jet, j_{all} refers to any jet in the event with $p_T > 15$ GeV, pseudorapidity $|\eta| < 3.2$ and without the taggability requirement. The thrust axis is the direction obtained from the difference of the transverse momenta of the leading and next-to-leading jets. The recoil is defined in the plane transverse to the beam using i) either the amount of missing transverse energy that remains after removal of the two leading jets, ii) or the sum of all good jet transerse momenta in the half plane opposite to the one containing the dijet system (with respect to the thrust axis). Among these two possible recoil definitions, the one that has the larger component along the direction orthogonal to the thrust is chosen.

Variables used in the MJ DT
$\Delta\phi(\text{jet}_1, \text{jet}_2)$
η of jet_1
$\not\!\!E_T$
$\not\!\!E_T$ significance
$\min \Delta\phi(\not\!\!E_T, j_{\text{all}})$
$\max \Delta\phi(\not\!\!E_T, j_{\text{all}}) + \min \Delta\phi(\not\!\!E_T, j_{\text{all}})$
$\max \Delta\phi(\not\!\!E_T, j_{\text{all}}) - \min \Delta\phi(\not\!\!E_T, j_{\text{all}})$
$\not\!\!H_T$(vectorial sum of j_{all} p_T)
$\not\!\!H_T / H_T$ (with H_T the scalar sum of j_{all} p_T)
Asymmetry between $\not\!\!E_T$ and $\not\!\!H_T$: $(\not\!\!E_T - \not\!\!H_T)/(\not\!\!E_T + \not\!\!H_T)$
$\not\!\!E_T$ component along the thrust axis
$\not\!\!E_T$ component perpendicular to the thrust axis
Sum of the signed components of the dijet and recoil momenta along the thrust axis
Sum of the signed components of the dijet and recoil momenta perpendicular to the thrust axis
Centrality (ratio of the scalar sum of jet_1 and jet_2 p_T to the sum of their energies)
θ angle of the dijet system
Polar angle of jet_1 boosted to the dijet rest frame with respect to the dijet direction in the laboratory
Variables used in the SM DT
Dijet mass
Dijet transverse mass
jet_1 p_T
jet_2 p_T
Scalar sum of jet_1 and jet_2 p_T
η of jet_1
η of jet_2
$\Delta\eta(\text{jet}_1, \text{jet}_2)$
$\Delta\phi(\text{jet}_1, \text{jet}_2)$
$\Delta R(\text{jet}_1, \text{jet}_2)$
p_T weighted $\Delta R(\text{jet}_1, j_{\text{all}})$
p_T weighted $\Delta R(\text{jet}_2, j_{\text{all}})$
H_T(scalar sum of j_{all} p_T)
$\not\!\!H_T$(vectorial sum of j_{all} p_T)
$\not\!\!H_T / H_T$
$\Delta\phi(\not\!\!E_T, \text{dijet})$
θ angle of jet_1 boosted to the dijet rest frame
Polar angle of jet_1 boosted to the dijet rest frame with respect to the dijet direction in the laboratory
$\min \Delta\phi(\not\!\!E_T, j_{\text{all}})$
$\max \Delta\phi(\not\!\!E_T, j_{\text{all}}) + \min \Delta\phi(\not\!\!E_T, j_{\text{all}})$
Dijet p_T
$\Delta\phi(\not\!\!E_T, \text{jet}_1)$

TABLE IV: Systematic uncertainties, in percent, of the overall signal and background yields. "Jet EC" and "Jet ER" stand for jet energy calibration and resolution respectively. "Jet R&T" stands for jet reconstruction and taggability. "Signal" includes ZH and WH production and is shown for $m_H = 125$ GeV.

Systematic Uncertainty	Signal (%)	Background (%)
Medium b-tag		
Jet EC - Jet ER	± 0.9	± 1.9
Jet R&T	± 2.9	± 2.9
b Tagging	± 0.6	± 3.7
Trigger	± 2.0	± 1.9
Lepton Identification	± 0.8	± 0.9
Heavy Flavor Fractions	–	± 8.5
Cross Sections	± 7.0	± 9.8
Luminosity	± 6.1	± 5.8
Multijet Normalilzation	–	± 1.2
Total	± 10.0	± 14.2
Tight b-tag		
Jet EC - Jet ER	± 1.0	± 1.8
Jet R&T	± 2.7	± 3.1
b Tagging	± 8.6	± 7.4
Trigger	± 2.0	± 2.0
Lepton Identification	± 0.9	± 1.1
Heavy Flavor Fractions	–	± 11.1
Cross Sections	± 7.0	± 10.0
Luminosity	± 6.1	± 6.1
Multijet Normalilzation	–	± 0.1
Total	± 13.2	± 16.9

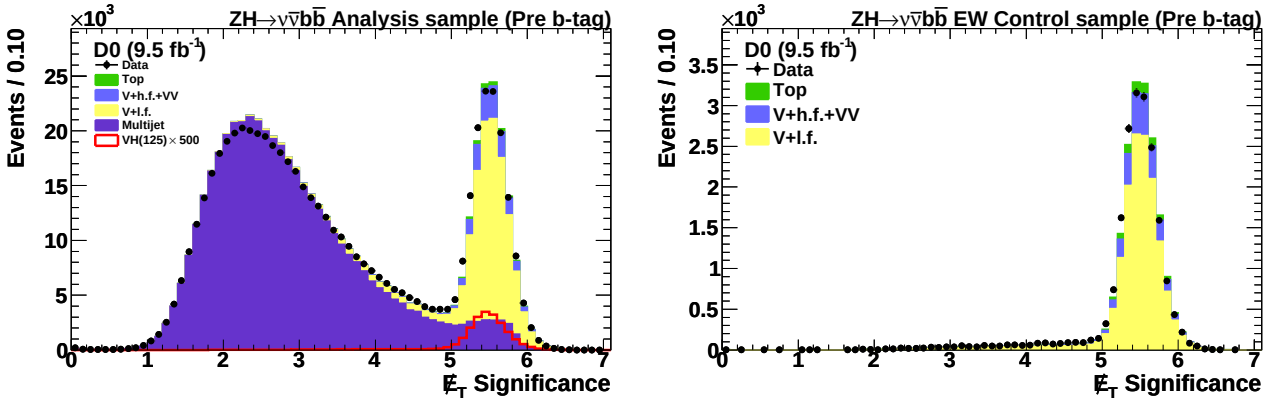

(a) (b)

FIG. 9: Missing E_T significance in (a) the analysis and (b) the EW-control samples without the requirement that the significance be larger than 5. The data are shown as points and the background contributions as histograms: dibosons are labeled as "VV," "V+l.f." includes $(W/Z)+(u,d,s,g)$ jets, "V+h.f." includes $(W/Z)+(b,c)$ jets and "Top" includes pair and single top quark production. In (a), the distribution for signal (VH) is multiplied by a factor of 500 and includes ZH and WH production for $m_H = 125$ GeV.

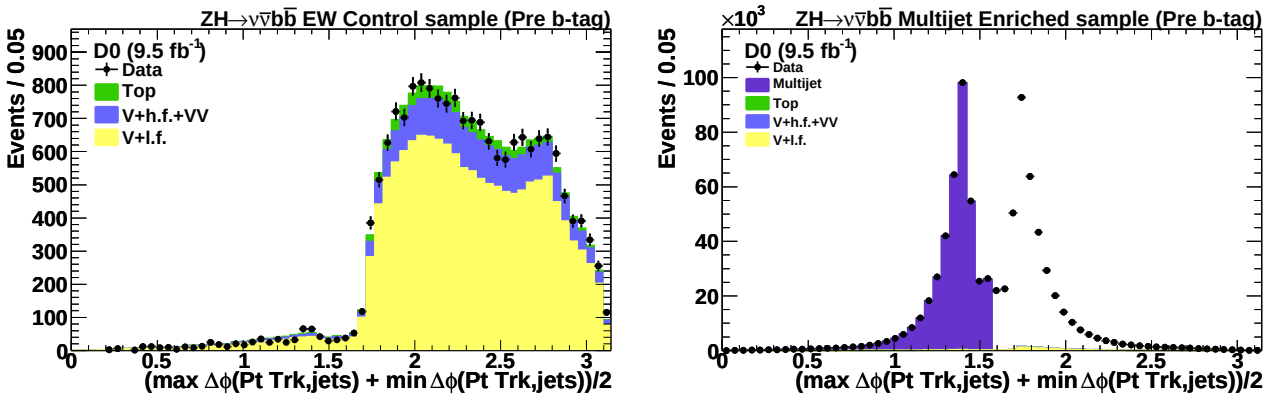

(a) (b)

FIG. 10: Distribution of $\mathcal{D}$ in (a) the EW-control sample and (b) the MJ-enriched sample, without the requirement that it be larger than $\pi/2$. The data are shown as points and the background contributions as histograms: dibosons are labeled as "VV," "V+l.f." includes $(W/Z)+(u,d,s,g)$ jets, "V+h.f." includes $(W/Z)+(b,c)$ jets and "Top" includes pair and single top quark production. In (b), the shaded region ($\mathcal{D} < \pi/2$) is used to model the events in the unshaded region ($\mathcal{D} > \pi/2$); the dip observed in the region around $\pi/2$ is due to the acoplanarity cut between the Higgs candidate jets. These distributions are shown before b tagging.

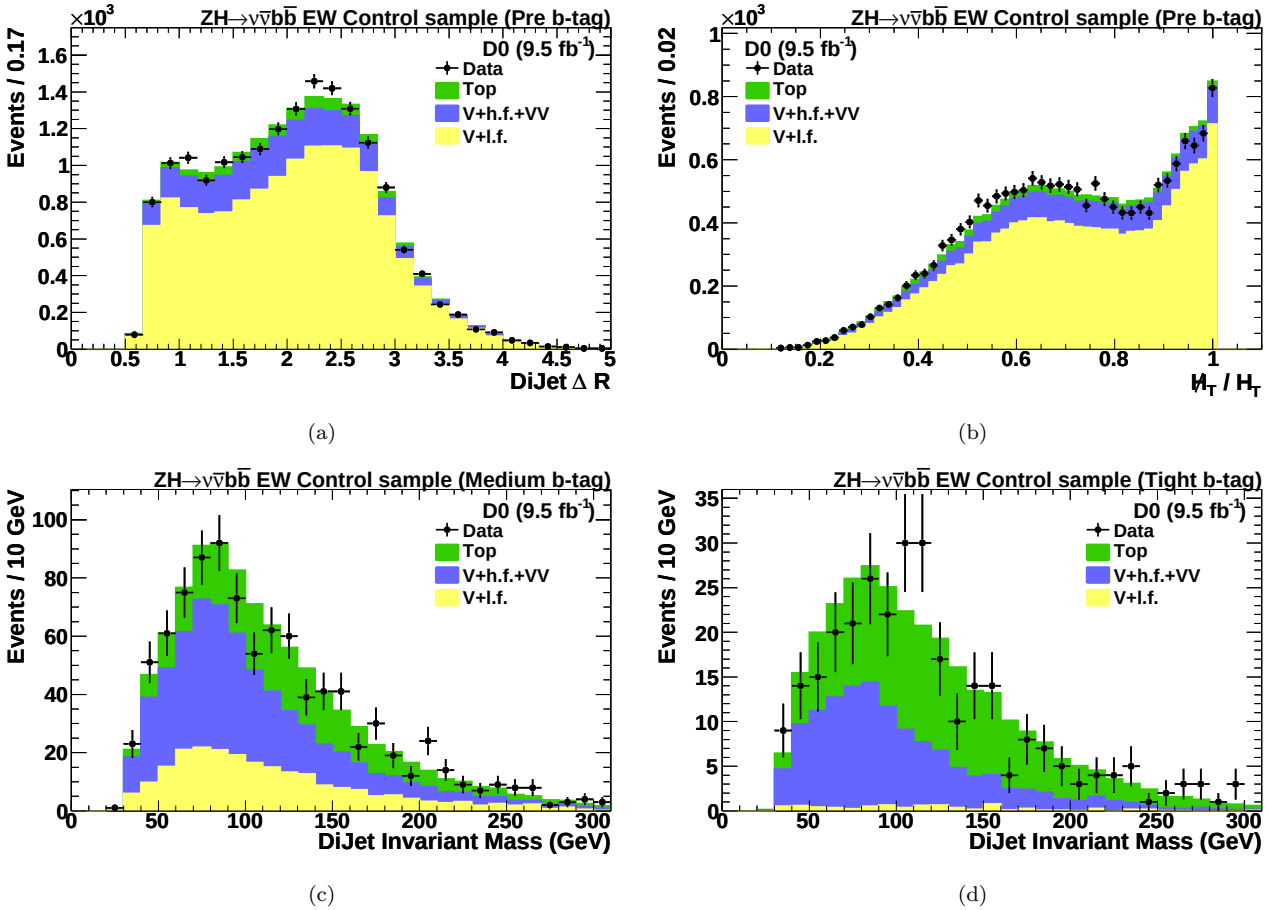

(a) (b) (c) (d)

FIG. 11: Representative variable distributions in the EW-control sample: (a) dijet ΔR in the pre b-tag sample, (b) $\not{H}_T/H_T$ (defined in Table I) in the pre b-tag sample, (c) dijet invariant mass in the medium b-tag sample, (d) dijet invariant mass in the tight b-tag sample. The data are shown as points and the background contributions as histograms: dibosons are labeled as "VV," "V+l.f." includes $(W/Z)+(u,d,s,g)$ jets, "V+h.f." includes $(W/Z)+(b,c)$ jets and "Top" includes pair and single top quark production.

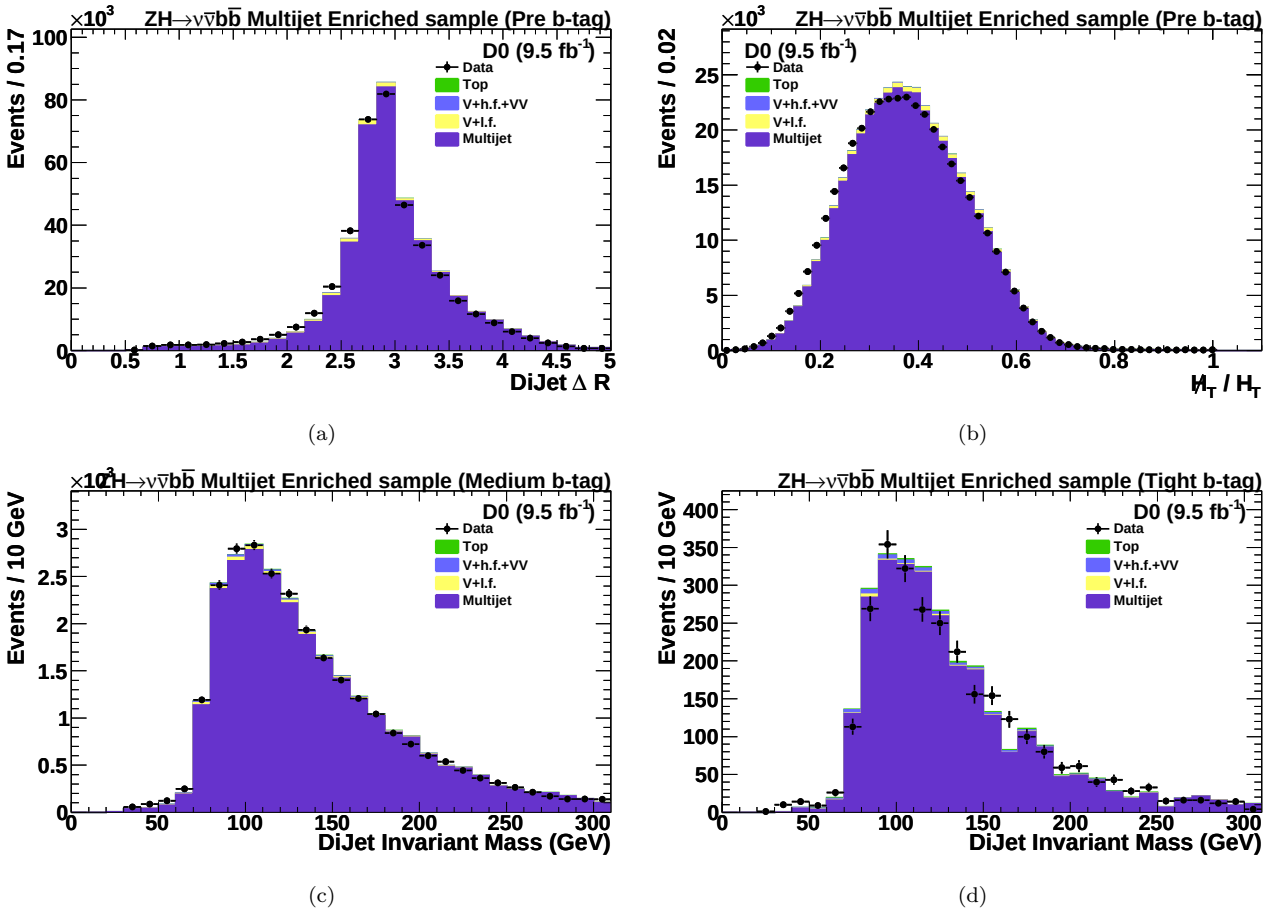

FIG. 12: Representative variable distributions in the MJ-enriched sample: (a) dijet ΔR in the pre b-tag sample, (b) $\not\!\!H_T/H_T$ (defined in Table I) in the pre b-tag sample, (c) dijet invariant mass in the medium b-tag sample, (d) dijet invariant mass in the tight b-tag sample. The data with $\mathcal{D} > \pi/2$ are shown as points and the background contributions as histograms: dibosons are labeled as "VV," "V+l.f." includes $(W/Z)+(u,d,s,g)$ jets, "V+h.f." includes $(W/Z)+(b,c)$ jets and "Top" includes pair and single top quark production. The "multijet" histogram is obtained from the data with $\mathcal{D} < \pi/2$

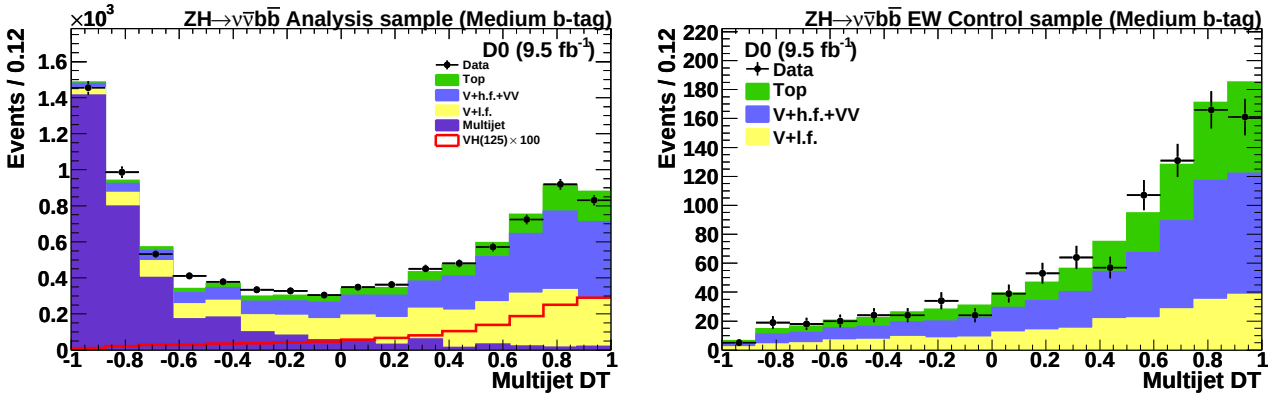

FIG. 13: MJ DT output after the medium b-tagging requirement in the (a) analysis sample and (b) EW-control sample. The distribution for signal (VH), shown for $m_H = 125$ GeV, is multiplied by a factor of 100 and includes ZH and WH production. The data are shown as points and the background contributions as histograms: dibosons are labeled as "VV," "V+l.f." includes $(W/Z)+(u,d,s,g)$ jets, "V+h.f." includes $(W/Z)+(b,c)$ jets and "Top" includes pair and single top quark production.

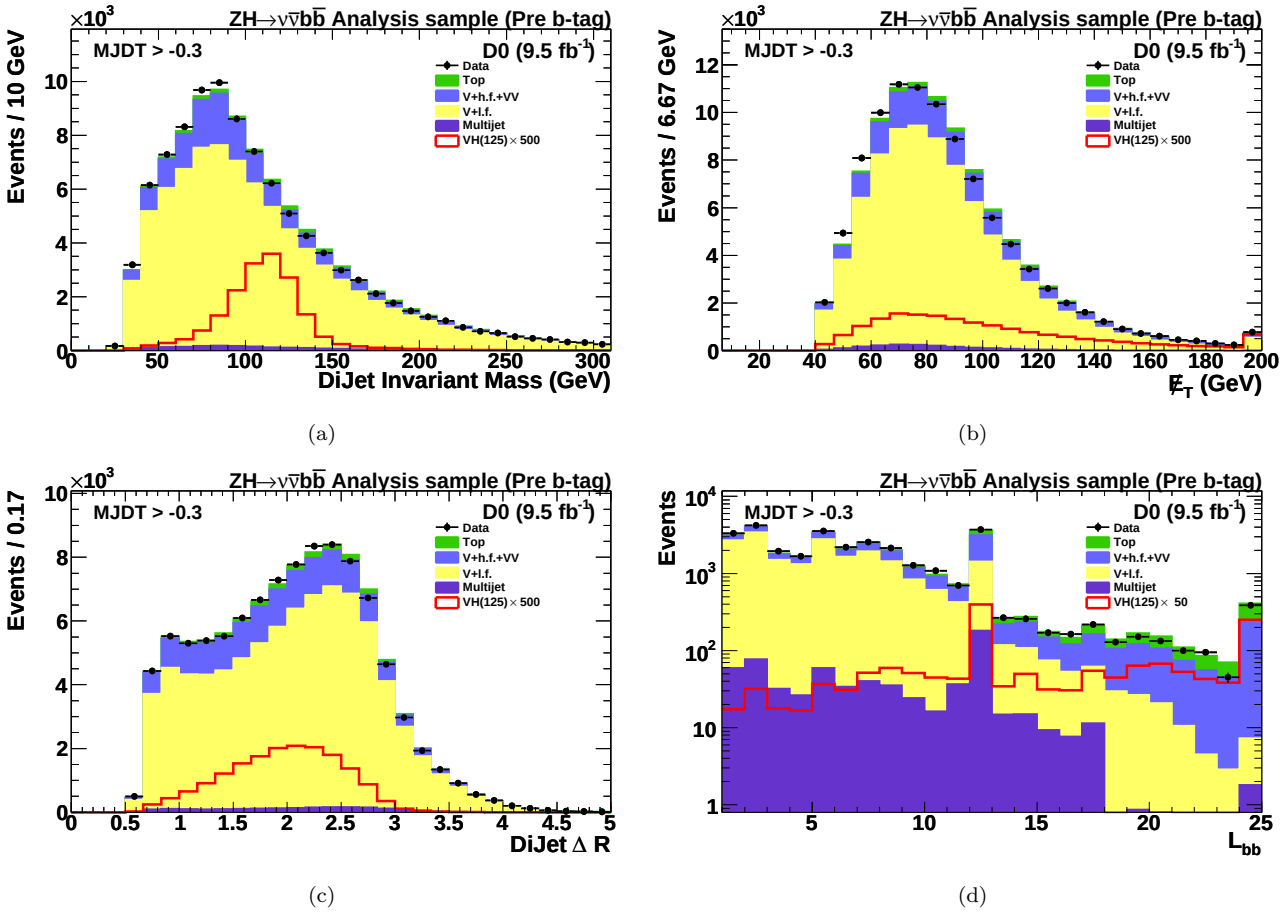

FIG. 14: Representative variable distributions in the analysis sample after the multijet veto and before any b tagging requirement: (a) dijet invariant mass, (b) missing E_T, (c) dijet ΔR, (d) b-tagging discriminating variable (L_{bb}). The bin at zero is surpressed in this plot due to the large number of entries, mostly from pairs of light jets. The relatively high number of events observed at $L_{bb} = 12$ comes mainly from events with one untagged jet and one very tightly b-tagged jet; the bin at $L_{bb} = 24$ comes from events with two very tightly b-tagged jets. The distributions for signal (VH), which are multiplied by a factor of 500 for (a)–(c) and 50 for (d), include ZH and WH production for $m_H = 125$ GeV. The data are shown as points and the background contributions as histograms: dibosons are labeled as "VV," "V+l.f." includes $(W/Z)+(u, d, s, g)$ jets, "V+h.f." includes $(W/Z)+(b, c)$ jets and "Top" includes pair and single top quark production.

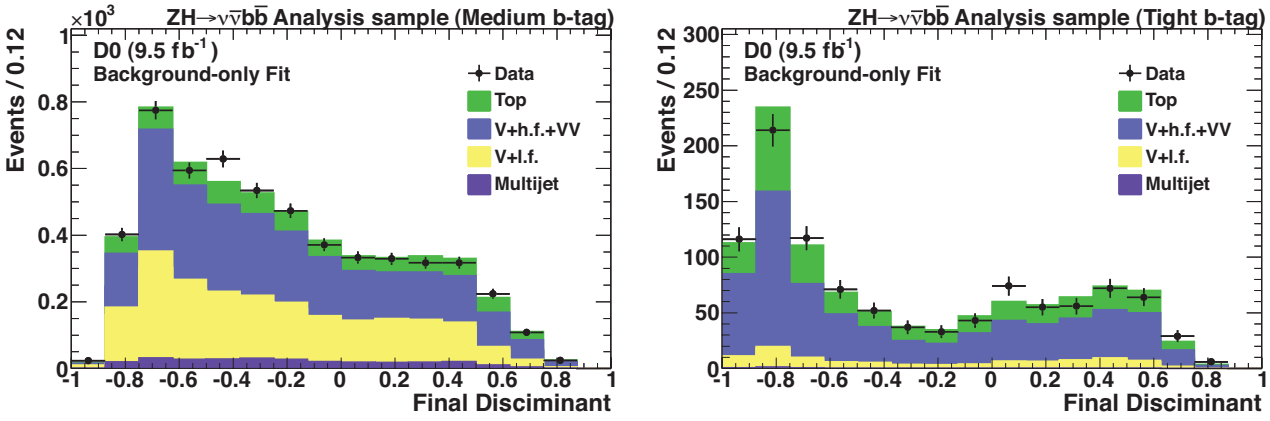

(a) (b)

FIG. 15: The SM DT output, for $m_H = 125$ GeV, following the multijet veto and after the fit to the data under the background-only hypothesis in the (a) medium and (b) tight b-tag channels. The data are shown as points and the background contributions as histograms: dibosons are labeled as "VV", "V+l.f." includes $(W/Z)+(u,d,s,g)$ jets, "V+h.f." includes $(W/Z)+(b,c)$ jets and "Top" includes pair and single top quark production.

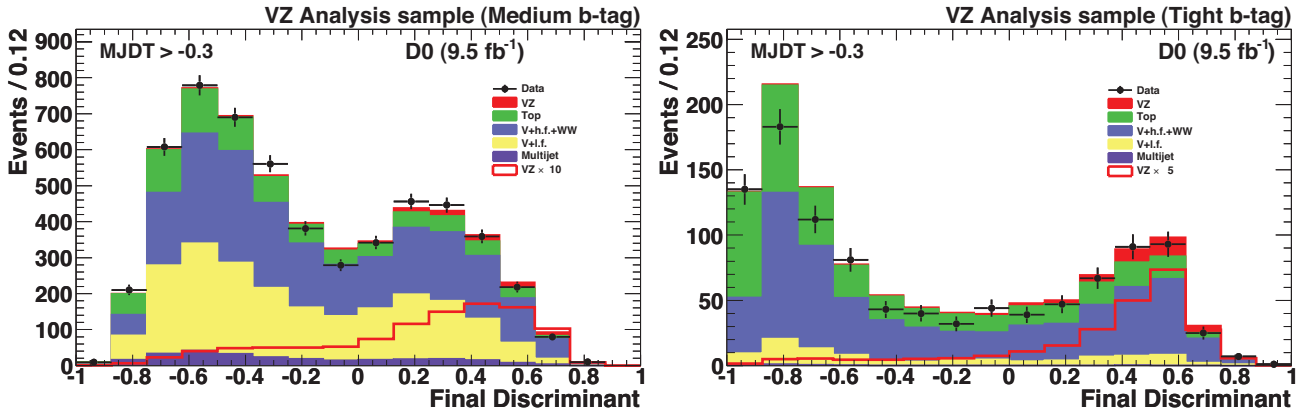

(a) (b)

FIG. 16: The SM DT output for the WZ and ZZ diboson search following the multijet veto for (a) medium and (b) tight tag prior to the fit to data. The data are shown as points and the background contributions as histograms; "V+l.f." includes $(W/Z)+(u,d,s,g)$ jets, "V+h.f." includes $(W/Z)+(b,c)$ jets and "Top" includes pair and single top quark production. The WZ and ZZ signal is denoted as VZ. The distributions for signal are scaled to the SM cross section (filled red histogram) and shown separately multiplied by a factor of 10 for medium b-tag and 5 for tight b-tag (solid red line) respectively.

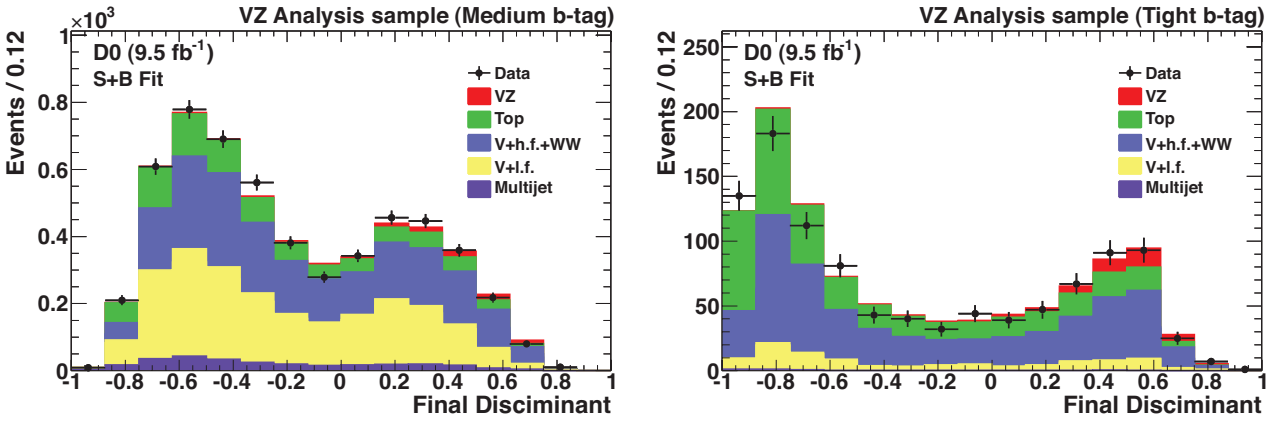

(a) (b)

FIG. 17: The SM DT output for the WZ and ZZ diboson search, following the multijet veto, and after the fit to the data under the signal+background hypothesis in the (a) medium and (b) tight tag channels. The data are shown as points and the background contributions as histograms; "V+l.f." includes $(W/Z)+(u,d,s,g)$ jets, "V+h.f." includes $(W/Z)+(b,c)$ jets and "Top" includes pair and single top quark production. The WZ and ZZ signal expectation (red histogram, and denoted VZ) is scaled to the SM cross section.

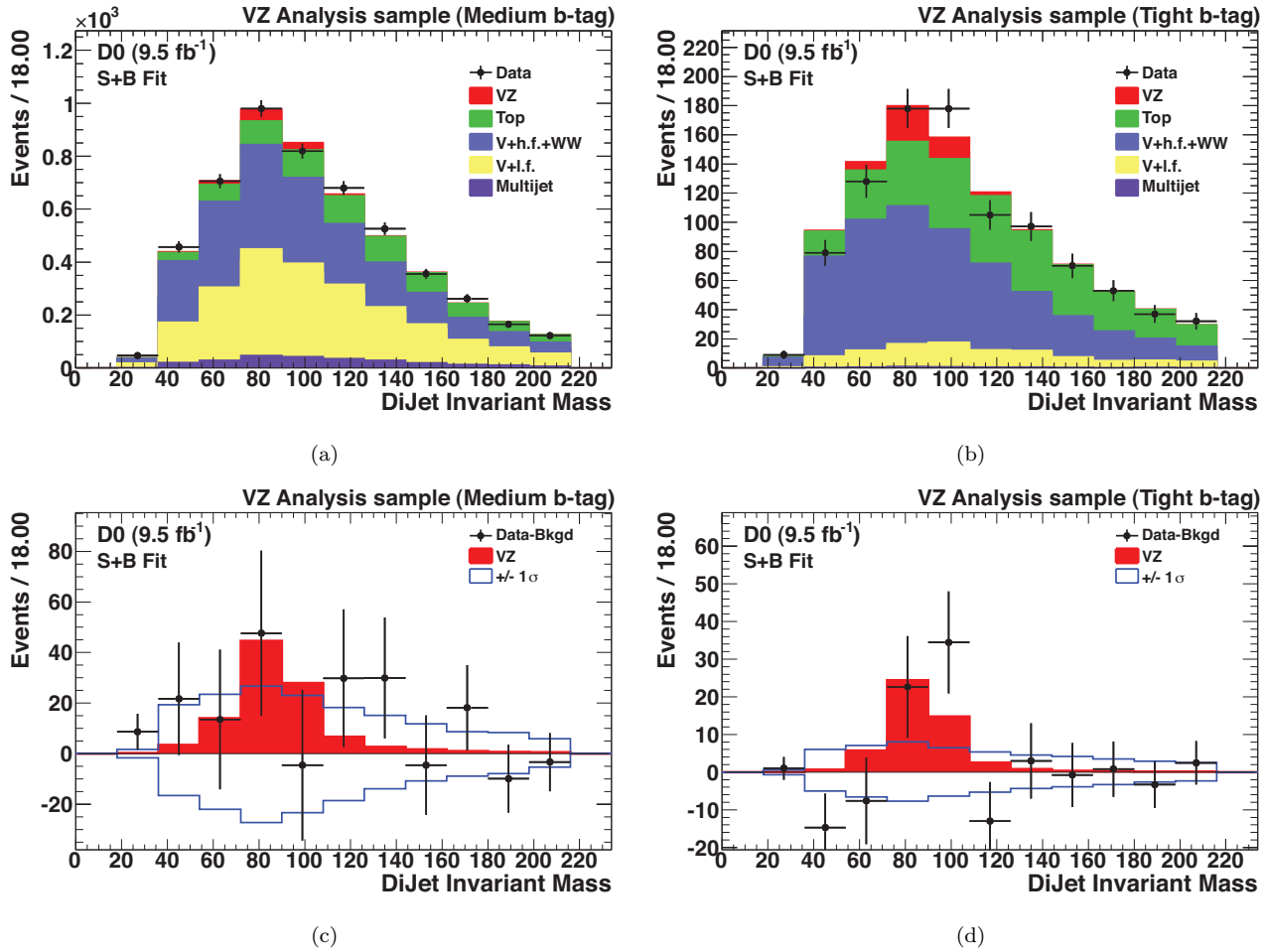

FIG. 18: The dijet invariant mass for the WZ and ZZ diboson search, following the multijet veto, and after the fit to the data under the signal+background hypothesis in the (a) medium and (b) tight tag channels. The data are shown as points and the background contributions as histograms; "V+l.f." includes $(W/Z)+(u,d,s,g)$ jets, "V+h.f." includes $(W/Z)+(b,c)$ jets and "Top" includes pair and single top quark production. The WZ and ZZ signal expectation (red histogram, and denoted VZ) and the data after subtracting the fitted background (points) are shown in the (c) medium and (d) tight tag channels. Also shown is the ± 1 standard deviation band on the total background after fitting. The signal is scaled to the SM cross section.